Journal of Materials Chemistry A

ROYAL SOCIETY OF CHEMISTRY

PAPER

View Article Online
View Journal | View Issue





Cite this: *J. Mater. Chem. A*, 2020, **8**, 6076

# $FeN_x$ and $\gamma$-$Fe_2O_3$ co-functionalized hollow graphitic carbon nanofibers for efficient oxygen reduction in an alkaline medium†

Qiang Yu,[a] Sitian Lian,[a] Jiantao Li,[a] Ruohan Yu,[ab] Shibo Xi,[c] Jinsong Wu,[b] Dongyuan Zhao,[a] Liqiang Mai[a] and Liang Zhou*[a]

Received 3rd January 2020
Accepted 2nd March 2020

DOI: 10.1039/d0ta00073f

rsc.li/materials-a

The exploration of efficient, stable, and inexpensive oxygen reduction reaction (ORR) electrocatalysts to replace Pt/C in fuel cells and metal–air batteries still remains an ongoing challenge. Herein, we report an efficient ORR electrocatalyst composed of single-atom $FeN_x$ and $\gamma$-$Fe_2O_3$ nanoparticle co-functionalized hollow graphitic carbon nanofibers ($FeN_x$/$Fe_2O_3$-CNFs). It is found that the $FeN_x$ species serve as the active sites, while the $\gamma$-$Fe_2O_3$ nanocrystals function as a co-catalyst to boost the ORR catalytic activity. The obtained $FeN_x$/$Fe_2O_3$-CNFs exhibit desirable ORR electrocatalytic activity with a 4-electron transfer pathway, a half-wave potential of 0.81 V approaching that of commercial Pt/C, low hydrogen peroxide yields (<6% at 0.2–0.7 V), long-term stability (87.14% after 30 000 s), and excellent methanol tolerance. The assembled Zn–air battery based on the $FeN_x$/$Fe_2O_3$-CNFs has an open circuit voltage of 1.51 V and superior energy density of 920 W h $kg^{-1}$. This work highlights the significant contribution of the co-catalyst in electrocatalysis.

## Introduction

The oxygen reduction reaction (ORR) has become a pivotal process in fuel cells and metal–air batteries.[1,2] Commercial Pt/C is currently the most widely employed ORR electrocatalyst. However, it suffers from high cost, scarcity, poor stability, and CO/methanol poisoning.[3–5] Hence, the exploration of alternative electrocatalysts with superior electrocatalytic activity, high stability, and low cost has become increasingly significant.[6–9]

Metal–nitrogen–carbon based materials (M–N–C, M = Fe, Co, *etc.*) have been identified as an alternative family of ORR electrocatalysts.[10–14] In 1964, Jasinski pioneered the employment of metal phthalocyanines, a family of macrocyclic complexes containing $M–N_4$ moieties, for the ORR.[15] Later, it was demonstrated that annealing $M–N_4$ containing compounds in an inert atmosphere could lead to a significantly improved ORR activity.[16] Recently, it was found that the pyrolysis of inexpensive C, N-containing precursors and transition metal species can also lead to M–N–C based ORR catalysts.[1,17–21] Since then, M–N–C has been extensively investigated.[22–31]

The composition of M–N–C catalysts is relatively complex and they usually contain N-doped carbon, $M–N_x$ moieties, and M-rich nanoparticles. Such complexity makes the real active sites and role of M-rich nanoparticles elusive.[32–36] It has been generally accepted that $M–N_x$ is the active sites for the ORR. A recent study by Wan *et al.* found that the Fe/$Fe_3C$ in Fe–N–C could boost the ORR performance of $FeN_x$.[34] That is to say, the Fe and/or $Fe_3C$ can function as a co-catalyst during the ORR process. A question arises: is there any other material which can act as a co-catalyst and boost the ORR activity of $M–N_x$ species like Fe or $Fe_3C$?

Herein, we report the construction of $FeN_x$ and $\gamma$-$Fe_2O_3$ nanoparticle co-functionalized hollow graphitic carbon nanofibers ($FeN_x$/$Fe_2O_3$-CNFs). It is found that the $\gamma$-$Fe_2O_3$ nanoparticles can function as a co-catalyst and effectively improve the ORR activity of $FeN_x$. The $FeN_x$/$Fe_2O_3$-CNFs exhibit a half-wave potential approaching that of commercial Pt/C. More importantly, the limiting current density and long-term stability of $FeN_x$/$Fe_2O_3$-CNFs in an alkaline medium surpass those of commercial Pt/C. This work highlights the significant contribution of the co-catalyst in electrocatalysis.

## Experimental

### Synthesis of $FeN_x$/$Fe_2O_3$-CNF and $FeN_x$/$Fe_3C$-CNF electrocatalysts

Phenolic resin nanofibers (RNFs) were synthesized based on our previous report.[37] Typically, the as-made RNF aerogel (0.3 g) and $Fe(NO_3)_3 \cdot 9H_2O$ (2.5 mmol) were dispersed in 50 mL water and

[a]State Key Laboratory of Advanced Technology for Materials Synthesis and Processing, Wuhan University of Technology, Wuhan 430070, P. R. China. E-mail: liangzhou@whut.edu.cn

[b]Nanostructure Research Centre, Wuhan University of Technology, Wuhan 430070, P. R. China

[c]Institute of Chemical and Engineering Sciences, A*STAR (Agency for Science, Technology and Research), Singapore 627833, Singapore

† Electronic supplementary information (ESI) available. See DOI: 10.1039/d0ta00073f

stirred at 25 °C for 24 h to allow the RNF to adsorb the ferric ions. After ferric ion adsorption, the sample was collected by centrifugation and freeze-dried. Subsequently, the sample was carbonized in $N_2$ at 800 °C for 1 h and treated with 0.5 M $H_2SO_4$ at 50 °C for 10 h to remove most of the Fe species. The sample was then subjected to pyrolysis at 800 °C for 2 h in $N_2$ or $H_2O/N_2$ to obtain the $FeN_x/Fe_3C$-CNFs and $FeN_x/Fe_2O_3$-CNFs, respectively.

### Characterization

The morphology of the samples was studied using a scanning electron microscope (SEM, JEOL-7100F) and transmission electron microscope (TEM, JEM-2100F and Titan Themis G2 60-300). The X-ray diffraction (XRD) patterns were collected on a Bruker D2 PHASER. The $N_2$ sorption results were obtained on a Tristar-3020 $N_2$ adsorption analyzer at 77 K. The surface compositions of the catalysts were analyzed using an X-ray photoelectron spectroscopy (XPS) instrument (VG MultiLab 2000). Thermogravimetric analysis (TGA) was performed on a NETZSCH STA 449F5 in air. Raman spectra were obtained by using a HORIBA LabRAM micro-Raman spectrometer. Mössbauer tests were conducted using a Wissel MS-500 spectrometer. A $^{57}Co$ (Rh) source with an activity of 25 mCi was employed. Velocity calibration was performed with a room temperature γ-Fe absorber. X-ray absorption near edge structure (XANES) and extended X-ray absorption fine structure (EXAFS) data were obtained at the XAFCA beamline of the Singapore Synchrotron Light Source.

### Electrochemical measurements

Electrochemical measurements were carried out with a CHI 760E workstation (Chenhua) in a standard three-electrode system. The well-dispersed inks were prepared by mixing 5 mg $FeN_x/Fe_2O_3$-CNFs and 5 mg Vulcan XC72R carbon, which were then added into 800 μL isopropanol, 150 μL deionized water, and 50 μL Nafion solution. After thorough ultrasonic treatment, 10 μL of the well-dispersed ink was dropped onto a glassy carbon electrode (GCE) surface with an area of 0.196 $cm^2$. A 0.1 M fresh $O_2$-saturated KOH solution was used as the electrolyte in all the ORR tests. The GCE, a Pt sheet, and a saturated calomel electrode (SCE) were used as the working electrode, counter electrode, and reference electrode, respectively. All potentials were calibrated to the reversible hydrogen electrode (RHE) on the basis of the Nernst equation: $E$ (RHE) = $E$ (SCE) + 0.0591 × pH + 0.241. Cyclic voltammetry (CV) and linear sweep voltammetry (LSV) curves were recorded at 5 and 10 mV $s^{-1}$, respectively. LSV curves at different rotation rates were obtained using a rotating disk-electrode (RDE). The electron transfer number ($n$) at different potentials was calculated based on the Koutecky–Levich (K–L) equation:

$$\frac{1}{J} = \frac{1}{J_K} + \frac{1}{0.62nFD_0^{2/3}C_0\,v^{-1/6}\omega^{1/2}}$$

where $J$ and $J_K$ are the measured current density and kinetic current density, respectively; $n$ stands for the electron transfer number; $F$ is the Faraday constant (96 500 C $mol^{-1}$); $C_0$ is the saturated concentration of $O_2$ in 0.1 M KOH ($1.2 \times 10^{-6}$ mol $cm^{-3}$); $D_0$ is the diffusion coefficient of the $O_2$ ($1.87 \times 10^{-6}$ $cm^2$ $s^{-1}$) solution; $v$ is the kinematic viscosity (0.01 $cm^2$ $s^{-1}$); and $\omega$ is the angular rotation rate of the electrode (rad $s^{-1}$).

The percentage of $H_2O_2$ and $n$ were also calculated using a rotating ring-disk electrode (RRDE) according to the following equations:

$$H_2O_2\ \% = 200\frac{I_r/N}{I_d + (I_r/N)}$$

$$n = \frac{4I_d}{I_d + (I_r/N)}$$

where $I_d$ and $I_r$ are the disk current and ring current, respectively. And $N$ is the current collection efficiency (0.37).

**Tolerance to methanol.** LSV curves at a rotation rate of 1600 rpm were obtained to evaluate the methanol tolerance of $FeN_x/Fe_2O_3$-CNFs and the Pt/C catalyst. 3 M methanol was injected into the alkaline medium.

**KSCN toxicity tests.** To investigate the effect of Fe–$N_x$ on the ORR activity of $FeN_x/Fe_2O_3$-CNFs, a 10 mM fresh KSCN solution was injected into the alkaline medium before the LSV tests.

**Zn–air battery assembly.** Zn–air batteries were constructed with a polished Zn plate (thickness: 0.25 cm) as the anode, hydrophobic carbon cloth (W1S1009, CeTech Co., Ltd) loaded with well-dispersed ink as the air cathode, and 6.0 M KOH as the electrolyte. The ink is the same as that in the above ORR test and the mass loading of the catalyst is 1 mg $cm^{-2}$. Zn–air battery performance was tested in air using a customized electrochemical cell.

## Results and discussion

The synthesis of $FeN_x/Fe_2O_3$-CNFs involves three major steps: (I) ferric ion adsorption, (II) carbonization, and (III) steam activation (Fig. 1). 3-Aminophenol–formaldehyde RNFs prepared by a scalable sol–gel method are employed as the precursor.[37] The abundant hydroxyl (−OH) and amino ($-NH_2$) groups on the surface of the RNFs (Fig. S1†) enable effective adsorption of ferric ions ($Fe^{3+}$). During carbonization at 800 °C, the ion species are partially reduced to $Fe_3C$ and the remaining ions can be stabilized by N, forming $FeN_x$ species. Meanwhile, the $Fe_3C$ catalyzes the conversion of RNFs into partially graphitic CNFs. Thus, the product after secondary carbonization is denoted as $FeN_x/Fe_3C$-CNFs. With steam activation at 800 °C, the Fe species facilitate further graphitization, the amorphous carbon is etched away by steam, and the $Fe_3C$ is oxidized to γ-$Fe_2O_3$. As a result, $FeN_x/Fe_2O_3$-CNFs are obtained.

The obtained RNFs exhibit a monolith morphology with ultralow density and can sit on a flower (Fig. 2a inset). SEM shows that the RNFs are composed of uniform nanofibers with a diameter of ~25 nm (Fig. 2a and S2†). After ferric ion adsorption, pyrolysis in $N_2$, and steam activation, their average diameter is reduced to ~20 nm and the surface becomes rough (Fig. 2b). TEM (Fig. 2c and S3†) and high-resolution TEM (HRTEM, Fig. 2d and e) images clearly reveal the hollow

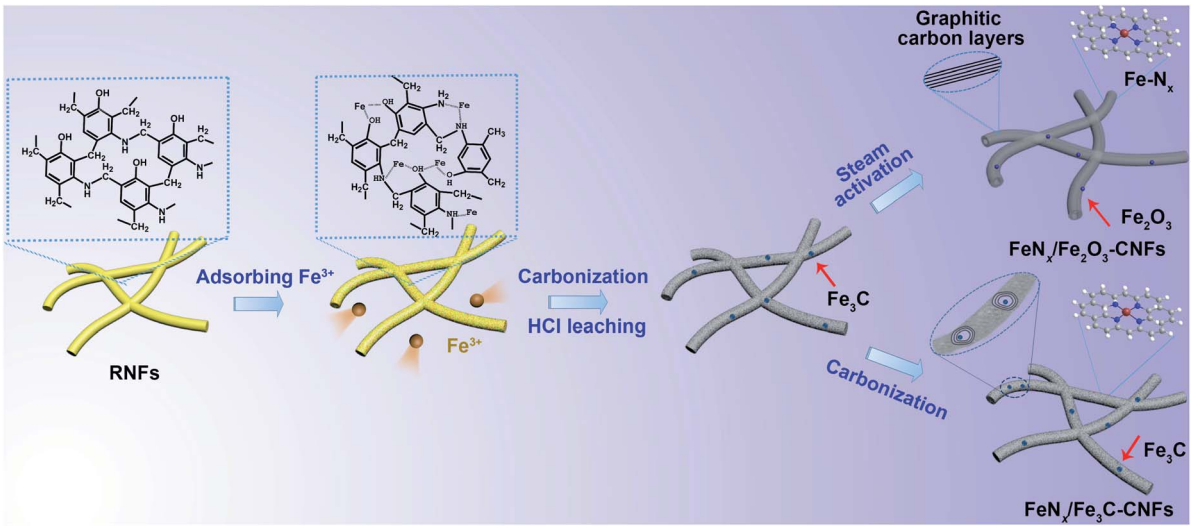


Fig. 1 Schematic illustration of the synthesis of $FeN_x$ and γ-$Fe_2O_3$ nanoparticle co-functionalized hollow graphitic carbon nanofibers ($FeN_x$/$Fe_2O_3$-CNFs).

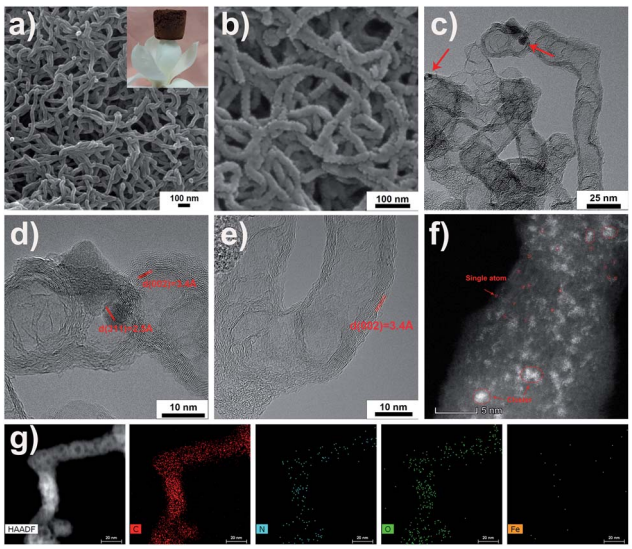


Fig. 2 The SEM image of resin nanofibers (a); SEM (b), TEM (c), and HRTEM (d and e) images of $FeN_x$/$Fe_2O_3$-CNFs; the HAADF-STEM image of $FeN_x$/$Fe_2O_3$-CNFs (f); EDS elemental maps of C, N, O, and Fe (g). The inset in (a) is the digital photo of the RNF monolith.

graphitic structure of $FeN_x$/$Fe_2O_3$-CNFs. The wall of the CNFs is composed of 8–14 graphitic layers with interlayer distances of 3.4 Å, corresponding to the (002) plane of graphitic carbon. γ-$Fe_2O_3$ nanoparticles can be clearly observed in the CNFs (Fig. 2d). The interplanar spacing (0.25 nm) observed in Fig. 2d agrees well with the (311) lattice spacing of γ-$Fe_2O_3$. Besides the γ-$Fe_2O_3$ nanoparticles, Fe species (both atomically dispersed Fe single atoms and few-atom clusters) can also be observed in other areas of the CNFs as shown in the high-angle annular dark-field scanning transmission electron microscopy image (HAADF-STEM, Fig. 2f). The Fe is also confirmed by energy dispersive X-ray spectroscopy (EDS) elemental mapping (Fig. 2g). As a single Fe-atom is unstable when exposed to air, it is speculated that the Fe species are stabilized by N-coordination and exist as $FeN_x$. From the above characterization, we tentatively term the sample $FeN_x$ and γ-$Fe_2O_3$ co-functionalized hollow graphitic carbon nanofibers ($FeN_x$/$Fe_2O_3$-CNFs).

For comparison, a sample without steam activation was also synthesized and characterized. It consists of $FeN_x$ and $Fe_3C$ co-functionalized CNFs ($FeN_x$/$Fe_3C$-CNFs, Fig. S4†). Direct carbonization of the RNFs leads to amorphous N-doped CNFs (Fig. S5†). Different from $FeN_x$/$Fe_2O_3$-CNFs, neither $FeN_x$/$Fe_3C$-CNFs nor N-doped CNFs have a hollow tubular structure, demonstrating that steam activation plays a significant role in forming the hollow structure. To further explore the reason for the formation of the hollow graphitic structure, the steam activation temperature is varied from 700 to 900 °C. The hollow graphitic structure begins to form at 700 °C (Fig. S6†) although most CNFs remain amorphous at this temperature. Most of the CNFs can be converted into hollow graphitic CNFs at 800 °C and the hollow graphitic CNF morphology is partially destroyed at 900 °C (Fig. S7†).

The XRD (Fig. 3a) pattern of the $FeN_x$/$Fe_2O_3$-CNFs shows two typical diffractions for γ-$Fe_2O_3$ (JCPDS no. 39-1346) and two diffractions for graphitic carbon (JCPDS no. 26-1079). As for $FeN_x$/$Fe_3C$-CNFs, the XRD pattern shows two diffractions for graphitic carbon, while no diffraction for $Fe_3C$ can be detected. The existence of $Fe_3C$ nanocrystals in $FeN_x$/$Fe_3C$-CNFs can only be demonstrated using the HRTEM image (Fig. S4c†). The high graphitization degree of $FeN_x$/$Fe_2O_3$-CNFs can be confirmed with the Raman spectra (Fig. S8†). The $FeN_x$/$Fe_2O_3$-CNFs show a relatively low $I_D/I_G$ ratio of 1.03, much lower than that of $FeN_x$/$Fe_3C$-CNFs (1.15).

The surface area and porosity were studied by $N_2$ sorption (Fig. S9†). The BET surface area and pore volume of $FeN_x$/$Fe_2O_3$-CNFs reach 712 $m^2$ $g^{-1}$ and 1.15 $cm^3$ $g^{-1}$ (Table S1†),

 

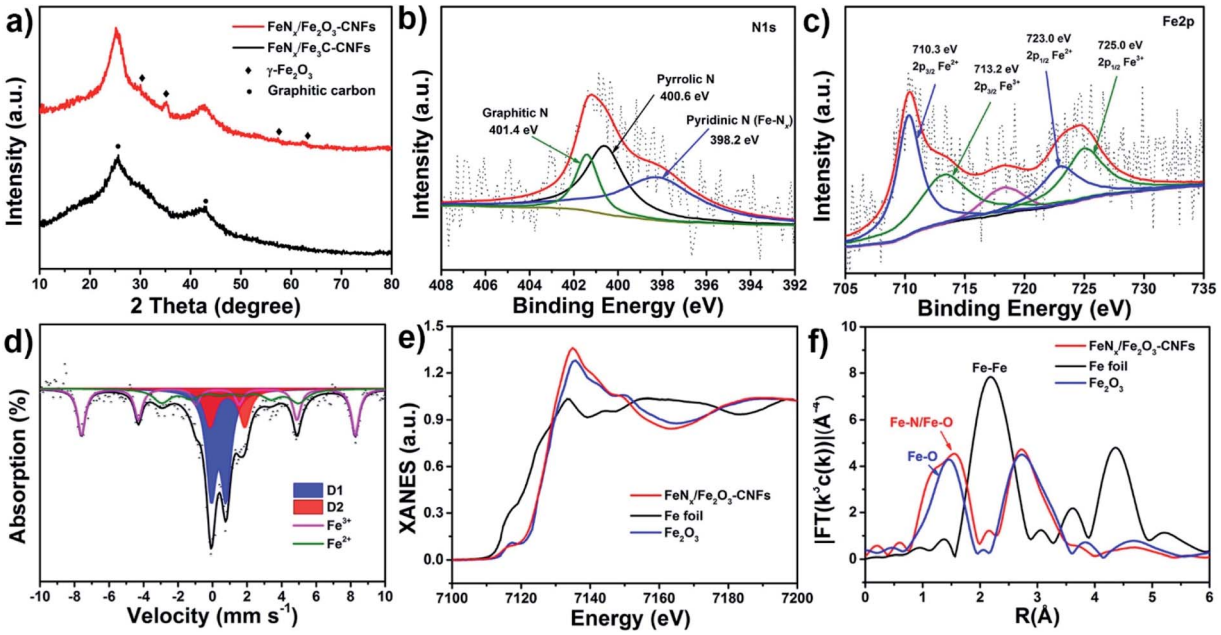


Fig. 3 XRD patterns (a) of $FeN_x/Fe_2O_3$-CNFs and $FeN_x/Fe_3C$-CNFs; high-resolution N1s (b) and Fe2p (c) XPS spectra of the $FeN_x/Fe_2O_3$-CNFs; $^{57}Fe$ Mössbauer spectrum of the $FeN_x/Fe_2O_3$-CNFs (d); Fe K-edge XANES (e) and FT $k^3$-weighted EXAFS spectra (f) of $FeN_x/Fe_2O_3$-CNFs, Fe foil and $Fe_2O_3$.

respectively. In addition, the *t*-Plot microporous surface area and pore volume of the $FeN_x/Fe_2O_3$-CNFs are calculated to be 308 $m^2\ g^{-1}$ and 0.16 $cm^3\ g^{-1}$, respectively. The (microporous) surface area and pore volume of $FeN_x/Fe_2O_3$-CNFs are slightly higher than those of $FeN_x/Fe_3C$-CNFs. In electrocatalysis, the higher surface area can expose more active sites and thus contribute to the $O_2$ adsorption and reduction effectively.

The XPS survey spectrum of $FeN_x/Fe_2O_3$-CNFs shows an Fe content of 0.35 wt% (Fig. S10†). TGA (Fig. S11†) in air shows a weight loss of ~85 wt%, corresponding to an Fe content of 10.5 wt%. The Fe content determined by XPS is far below that measured by TGA. This is because most of the Fe species are encapsulated in graphitic carbon shells, making them difficult to detect using the XPS technique. The high-resolution N 1s spectrum (Fig. 3b) shows three types of N species: pyridinic-N or Fe–$N_x$ species (398.2 eV), pyrrolic-N (400.6 eV), and graphitic-N (401.4 eV).[7,38–40] Remarkably, the content of pyridinic-N reaches as high as 46.56%, which can effectively improve the activity of the catalyst and endow it with excellent surface wettability and onset potential, while the graphitic-N (16.43%) is beneficial for the improvement of diffusion-limited performance.[41] The high-resolution Fe 2p spectrum of $FeN_x/Fe_2O_3$-CNFs (Fig. 3c) can be deconvoluted into five components: the $2p_{3/2}$–$2p_{1/2}$ spin–orbit doublet for $Fe^{2+}$ at 710.3 and 723.0 eV, the $2p_{3/2}$–$2p_{1/2}$ spin–orbit doublet for $Fe^{3+}$ at 713.2 and 725.0 eV, and the satellite peak at 717.2 eV. It should be noted that the peak at 710.3 eV can also be assigned to the $FeN_x$ species owing to the slight difference in binding energy between $FeN_x$ and pyridinic-N.[42,43] The $^{57}Fe$ Mössbauer spectrum of $FeN_x/Fe_2O_3$-CNFs can be fitted into four components (Fig. 3d). The D1 and D2 doublets can be assigned to $FeN_x$ species attributed to a low and medium spin state, respectively,[44,45] while the other two sextets are mainly from $Fe^{2+}$ and $Fe^{3+}$ species, suggesting the co-existence of $FeN_x$ and γ-$Fe_2O_3$ in hollow graphitic CNFs. The $FeN_x$ species, which are believed to be active sites for the ORR, account for 54.7% of the total Fe (Table S2†).

X-ray absorption spectroscopy was further conducted to analyze the atomic and electronic structure of Fe species in $FeN_x/Fe_2O_3$-CNFs. The Fe K-edge XANES (Fig. 3e) spectrum exhibits an absorption edge close to that of $Fe_2O_3$, suggesting the $Fe^{3+}$ valence state of Fe species in $FeN_x/Fe_2O_3$-CNFs. Besides, the appearance of a weak pre-edge peak at ~7117 eV suggests the existence of the $FeN_x$ structure. The Fourier-transformed (FT) $k^3$-weighted EXAFS (Fig. 3f) spectrum of $FeN_x/Fe_2O_3$-CNFs exhibits a strong peak for Fe–N/O bonds at ~1.5 Å. It should be noted that the bond distance between Fe–N and Fe–O is very small, and the peak of $FeN_x/Fe_2O_3$-CNFs is obviously wider than that of $Fe_2O_3$ at ~1.5 Å. In general, the XANES and EXAFS results are well consistent with the HAADF-STEM, XPS, and Mössbauer spectroscopy characterization results. All these characterizations demonstrate the existence of $FeN_x$ in $FeN_x/Fe_2O_3$-CNFs.

The obtained $FeN_x/Fe_2O_3$-CNFs were confirmed to have superb ORR properties due to their unique structure with a one dimensional (1D) nanostructure, high graphitization degree, high surface areas, and well-dispersed $FeN_x$ species. The CV (Fig. S12†) curves of $FeN_x/Fe_2O_3$-CNFs and $FeN_x/Fe_3C$-CNFs show an oxygen reduction peak at 0.83 V (*vs.* RHE), more positive than that of N-doped CNFs (0.71 V). The LSV (Fig. 4a) curve of the $FeN_x/Fe_2O_3$-CNFs shows a half-wave potential ($E_{1/2}$) of 0.81 V. This $E_{1/2}$ is higher than those of N-doped CNFs (0.70 V) and $FeN_x/Fe_3C$-CNFs (0.79 V), and is only 17 mV lower than that

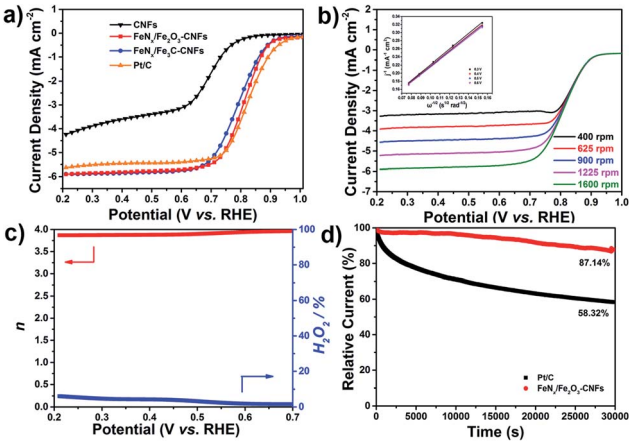


Fig. 4 LSV curves of $FeN_x/Fe_2O_3$-CNFs, $FeN_x/Fe_3C$-CNFs, Pt/C, and CNFs in $O_2$-saturated 0.1 M KOH (1600 rpm at 10 mV $s^{-1}$) (a); LSV curves of $FeN_x/Fe_2O_3$-CNFs at rotation rates from 400 to 1600 rpm (inset: the corresponding K–L plots) (b); electron transfer number and $H_2O_2$ yields of $FeN_x/Fe_2O_3$-CNFs at 0.2–0.7 V (c); stability tests of $FeN_x/Fe_2O_3$-CNFs and Pt/C at 0.75 V (d).

of commercial 20 wt% Pt/C. In addition, the $FeN_x/Fe_2O_3$-CNFs show the highest limiting current density ($I_{limit} = \sim 6$ mA $cm^{-2}$) among all the catalysts, which is close to the theoretical value at 1600 rpm and suggests rapid mass-transfer kinetics. In the kinetic control region (0.9 V), the $J_k$ of $FeN_x/Fe_2O_3$-CNFs reaches 0.50 mA $cm^{-2}$, which is close to that of Pt/C. The effects of activation temperature on ORR performance have been evaluated by varying the activation temperature from 700 to 900 °C. Both the CV and LSV results demonstrate that the sample activated at 800 °C outperforms that prepared at 700 and 900 °C (Fig. S13†). Although the sample prepared at 900 °C shows the highest surface area, the hollow graphitic CNF structure is partially destroyed owing to over activation, leading to a decrease in catalytic performance.

To investigate the electron transfer number ($n$) during the ORR, LSV curves at various rotation rates were recorded (Fig. 4b). Due to the decreased diffusion distance at high rotation speeds, the $I_{limit}$ increases proportionally with the rotation speed. The K–L plots show perfect linearity at various potentials. The $n$ is determined to be ~4 for $FeN_x/Fe_2O_3$-CNFs, demonstrating a direct 4-electron reduction ORR pathway. The peroxide species yields and corresponding $n$ of $FeN_x/Fe_2O_3$-CNFs were also determined by RRDE tests. The $H_2O_2$ yields of $FeN_x/Fe_2O_3$-CNFs remain below 6% in the potential range of 0.2–0.7 V (Fig. 4c), confirming a direct 4-electron transfer pathway for the ORR. When compared to $FeN_x/Fe_3C$-CNFs, the $FeN_x/Fe_2O_3$-CNFs exhibit lower $H_2O_2$ yields and a higher electron transfer number (Fig. S14†). Thus, the high ORR activity of $FeN_x/Fe_2O_3$-CNFs is proved by the 4-electron reduction of oxygen and the very low $H_2O_2$ yields. The obtained $FeN_x/Fe_2O_3$-CNF catalyst also demonstrates outstanding methanol tolerance performance (Fig. S15†). With the addition of methanol, the LSV curve of $FeN_x/Fe_2O_3$-CNFs presents no obvious change, while the LSV curve of Pt/C shows a sharp deformation. Long-term stability is another key parameter for ORR catalysts. During the stability test (30 000 seconds), the $FeN_x/Fe_2O_3$-CNFs show a slight current loss of 12.86% (Fig. 4d). Under the same conditions, the commercial Pt/C loses 41.68% of its activity.

Considering the complexity of the catalyst, an $SCN^-$ poisoning experiment was performed to block the Fe–$N_x$ species. After injecting KSCN, the ORR activity of $FeN_x/Fe_2O_3$-CNFs was significantly degraded, demonstrating the active role of Fe–$N_x$ in the ORR (Fig. S16†). This is well consistent with previous reports which showed that Fe–$N_x$ species were the active sites of Fe–N–C catalysts for the ORR.[29,46–50] In fact, a recent study by Wan *et al.* demonstrated that the Fe/$Fe_3C$ could boost the ORR activity of Fe–$N_x$.[34] In the present study, the $Fe_3C$ nanoparticles are converted into γ-$Fe_2O_3$ nanocrystals *via* a facile steam treatment. And we found that the γ-$Fe_2O_3$ nanocrystals can also act as a co-catalyst for the ORR and are even more effective than $Fe_3C$ in boosting the activity of Fe–$N_x$. Although the origin of enhanced ORR activity is not clear at this stage, it is speculated that there may exist certain interactions between the $Fe_2O_3$ nanocrystals and neighboring $FeN_x$, say alteration of the Fe's charge density. Further studies, such as density functional theory calculations, will be performed in the future to help us understand the role of $Fe_2O_3$ in the Fe–N–C catalyst in the ORR in detail.

Inspired by the excellent ORR performance, aqueous Zn–air batteries were assembled based on the $FeN_x/Fe_2O_3$-CNF catalyst using 6.0 M KOH as the electrolyte. As shown in Fig. 5a, the open circuit voltage (OCV) of the Zn–air battery based on $FeN_x/Fe_2O_3$-CNFs reaches 1.51 V, which is slightly higher than that of the battery based on the commercial Pt/C catalyst (1.48 V). The constructed devices also show good OCV stability after 1800 s. From the discharge polarization curve (Fig. 5b), the maximum current density and power density of the $FeN_x/Fe_2O_3$-CNF based battery are calculated to be 152.87 mA $cm^{-2}$ and 69.42 mW $cm^{-2}$, respectively. Both values are higher than those of the battery based on the Pt/C catalyst. In addition, the Zn–air

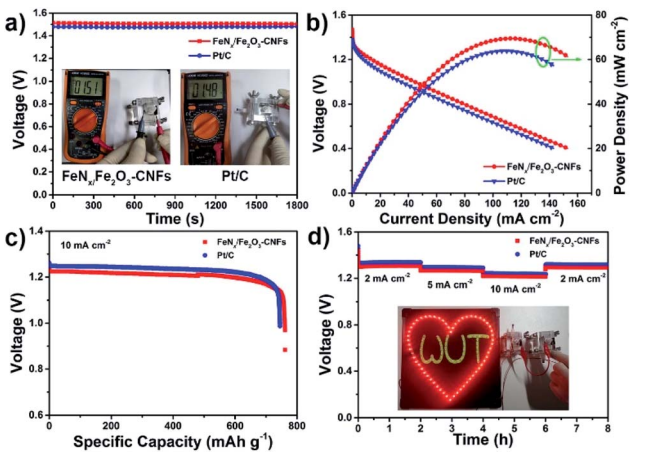


Fig. 5 Zn–air battery performances based on $FeN_x/Fe_2O_3$-CNFs and Pt/C catalysts. OCV stability (a); the insets show digital photos of the OCV; discharge polarization and corresponding power density curves (b); discharge curves at 10 mA $cm^{-2}$ (c); rate performance at different current densities (d); the inset shows a digital photo of 60 LEDs powered by two aqueous Zn–air batteries in series.

 

battery also exhibits a stable discharge curve with a voltage platform of ~1.21 V. At a current density of 10 mA $cm^{-2}$, the discharge capacity normalized to consumed Zn is up to 761 mA h $g^{-1}$, corresponding to an energy density of 920 W h $kg^{-1}$ (Fig. 5c). Although the average discharge voltage of the Pt/C based Zn–air battery reaches ~1.23 V, its specific capacity (744 mA h $g^{-1}$) and energy density (915 W h $kg^{-1}$) are slightly lower. Moreover, the rate performance of the Zn–air battery was tested at current densities of 2–10 mA $cm^{-2}$ (Fig. 5d). The Zn–air battery shows a very stable discharge voltage platform, and the discharge voltage decreases slowly with the increase of current density. When the current density returns to 2 mA $cm^{-2}$, the voltage platform can return to the initial level. It is worth mentioning that Zn–air batteries in series can successfully light up 60 LEDs, indicating the excellent practical application potential.

## Conclusions

In summary, we have constructed a highly efficient ORR catalyst consisting of $FeN_x$ single-atom and γ-$Fe_2O_3$ nanocrystal co-functionalized hollow graphitic carbon nanofibers ($FeN_x$/$Fe_2O_3$-CNFs). Featuring $FeN_x$ active sites, γ-$Fe_2O_3$ nanocrystals as the co-catalyst, and a 1D hollow graphitic CNF structure, the resultant $FeN_x$/$Fe_2O_3$-CNFs show superior ORR activity in terms of the 4-electron transfer pathway and low hydrogen peroxide yields. Besides, the high limiting current density, long-term stability, and excellent methanol tolerance of $FeN_x$/$Fe_2O_3$-CNFs are also competitive among those of previously reported M–N–C electrocatalysts. The assembled Zn–air battery based on $FeN_x$/$Fe_2O_3$-CNFs exhibits a high open circuit voltage, power density, and energy density. The present research highlights the important role of the co-catalyst in electrocatalysts.

## Conflicts of interest

There are no conflicts to declare.

## Acknowledgements

This work was supported by the National Natural Science Foundation of China (21673171), the Programme of Introducing Talents of Discipline to Universities (B17034), and the National Natural Science Fund for Distinguished Young Scholars (51425204).

## References

1 X. L. Tian, X. Zhao, Y. Q. Su, L. J. Wang, H. M. Wang, D. Dang, B. Chi, H. F. Liu, E. Hensen, X. W. Lou and B. Y. Xia, *Science*, 2019, **366**, 850–856.
2 F. Cheng and J. Chen, *Chem. Soc. Rev.*, 2012, **41**, 2172.
3 J. Zhang, K. Sasaki, E. Sutter and R. R. Adzic, *Science*, 2007, **315**, 220–222.
4 J. T. Zhang, Z. H. Zhao, Z. H. Xia and L. M. Dai, *Nat. Nanotechnol.*, 2015, **10**, 444–452.
5 Y. H. Bing, H. S. Liu, L. Zhang, D. Ghosh and J. J. Zhang, *Chem. Soc. Rev.*, 2010, **39**, 2184–2202.
6 J. Liang, R. F. Zhou, X. M. Chen, Y. H. Tang and S. Z. Qiao, *Adv. Mater.*, 2014, **26**, 6074–6079.
7 H. W. Liang, W. Wei, Z. S. Wu, X. Feng and K. Mullen, *J. Am. Chem. Soc.*, 2013, **135**, 16002–16005.
8 M. R. Benzigar, S. N. Talapaneni, S. Joseph, K. Ramadass, G. Singh, J. Scaranto, U. Ravon, K. Al-Bahilyc and A. Vinu, *Chem. Soc. Rev.*, 2018, **47**, 2680–2721.
9 J. C. Li, P. X. Hou, S. Y. Zhao, C. Liu, D. M. Tang, M. Cheng, F. Zhang and H. M. Cheng, *Energy Environ. Sci.*, 2016, **9**, 3079–3084.
10 F. Jaouen, E. Proietti, M. Lefèvre, R. Chenitz, J. P. Dodelet, G. Wu, H. T. Chung, C. M. Johnston and P. Zelenay, *Energy Environ. Sci.*, 2011, **4**, 114–130.
11 C. Guan, A. Sumboja, W. J. Zang, Y. H. Qian, H. Zhang, X. M. Liu, Z. L. Liu, D. Zhao, S. J. Pennycook and J. Wang, *Energy Storage Materials*, 2019, **16**, 243–250.
12 Y. Y. Xu, P. L. Deng, G. D. Chen, J. X. Chen, Y. Yan, K. Qi, H. F. Liu and B. Y. Xia, *Adv. Funct. Mater.*, 2019, 1906081.
13 G. Saianand, A.-I. Gopalan, J.-C. Lee, C. I. Sathish, K. Gopalakrishnan, G. E. Unni, D. Shanbhag, V. D. B. C. Dasireddy, J. Yi, S. B. Xi, A. Al-Muhtaseb and A. Vinu, *Small*, 2019, 1903937.
14 B. Y. Guan, L. Yu and X. W. Lou, *Adv. Sci.*, 2017, **4**, 1700247.
15 R. Jasinski, *Nature*, 1964, **201**, 1212–1213.
16 P. Neta, *J. Phys. Chem.*, 1981, **85**, 3678–3684.
17 S. Gupta, D. Tryk, I. Bae, W. Aldred and E. Yeager, *J. Appl. Electrochem.*, 1989, **19**, 19–27.
18 W. Gang, K. L. More, C. M. Johnston and Z. Piotr, *Science*, 2011, **332**, 443–447.
19 B. Y. Guan, Y. Lu, Y. Wang, M. H. Wu and X. W. Lou, *Adv. Funct. Mater.*, 2018, **28**, 1706738.
20 R. Jiang, L. Li, T. Sheng, G. Hu, Y. Chen and L. Wang, *J. Am. Chem. Soc.*, 2018, **140**, 11594–11598.
21 Z. Qiao, S. Hwang, X. Li, C. Wang, W. Samarakoon, S. Karakalos, D. Li, M. Chen, Y. He, M. Wang, Z. Liu, G. Wang, H. Zhou, Z. Feng, D. Su, J. S. Spendelow and G. Wu, *Energy Environ. Sci.*, 2019, **12**, 2830–2841.
22 K. L. Ai, Y. L. Liu, C. P. Ruan, L. H. Lu and G. Q. Lu, *Adv. Mater.*, 2013, **25**, 998–1003.
23 D. H. Deng, L. Yu, X. Q. Chen, G. X. Wang, L. Jin, X. L. Pan, J. Deng, G. Q. Sun and X. H. Bao, *Angew. Chem., Int. Ed.*, 2013, **52**, 371–375.
24 Q. Wang, Z. Y. Zhou, Y. J. Lai, Y. You, J. G. Liu, X. L. Wu, E. Terefe, C. Chen, L. Song, M. Rauf, N. Tian and S. G. Sun, *J. Am. Chem. Soc.*, 2014, **136**, 10882–10885.
25 M. Q. Wang, W. H. Yang, H. H. Wang, C. Chen, Z. Y. Zhou and S. G. Sun, *ACS Catal.*, 2014, **4**, 3928–3936.
26 Y. Hu, J. O. Jensen, W. Zhang, N. C. Lars, W. Xing, J. B. Niels and Q. F. Li, *Angew. Chem., Int. Ed.*, 2014, **126**, 3749–3753.
27 W. X. Yang, X. J. Liu, X. Y. Yue, J. B. Jia and S. J. Guo, *J. Am. Chem. Soc.*, 2015, **137**, 1436.
28 F. L. Meng, Z. L. Wang, H. X. Zhong, J. Wang, J. M. Yan and X. B. Zhang, *Adv. Mater.*, 2016, **28**, 7948–7955.
29 Z. Huang, H. Pan, W. Yang, H. Zhou, N. Gao, C. Fu, S. Li, H. Li and Y. Kuang, *ACS Nano*, 2018, **12**, 208–216.

30 B. C. Hu, Z. Y. Wu, S. Q. Chu, H. W. Zhu, H. W. Liang, J. Zhang and S. H. Yu, *Energy Environ. Sci.*, 2018, **11**, 2208–2215.
31 S. H. Wang, X. Yan, K. H. Wu, X. Chen, J. M. Feng, P. Y. Lu, H. Feng, H. M. Cheng, J. Liang and S. X. Dou, *Carbon*, 2019, **144**, 798–804.
32 Y. Zhu, B. Zhang, X. Liu, D. W. Wang and D. S. Su, *Angew. Chem., Int. Ed.*, 2014, **126**, 10849–10853.
33 A. Zitolo, V. Goellner, V. Armel, M. T. Sougrati, T. Mineva, L. Stievano, E. Fonda and F. Jaouen, *Nat. Mater.*, 2015, **14**, 937.
34 W. Jiang, L. Gu, L. Li, Y. Zhang, X. Zhang, L. Zhang, J. Wang, J. Hu, Z. Wei and L. Wan, *J. Am. Chem. Soc.*, 2016, **138**, 3570.
35 E. F. Holby, G. Wu, P. Zelenay and C. D. Taylor, *J. Phys. Chem. C*, 2014, **118**, 14388–14393.
36 H. Fei, J. Dong, Y. Feng, C. S. Allen, C. Wan, B. Volosskiy, M. Li, Z. Zhao, Y. Wang and H. Sun, *Nat. Catal.*, 2018, **1**, 63–72.
37 Q. Yu, J. Lv, Z. Liu, M. Xu, W. Yang, K. A. Owusu, L. Mai, D. Zhao and L. Zhou, *Sci. Bull.*, 2019, **64**, 1617–1624.
38 C. Zhu, S. Fu, J. Song, Q. Shi, D. Su, M. H. Engelhard, X. Li, D. Xiao, D. Li, L. Estevez, D. Du and Y. Lin, *Small*, 2017, **13**, 1603407.
39 Z. Y. Yang, Y. X. Zhang, L. Jing, Y. F. Zhao, Y. M. Yan and K. N. Sun, *J. Mater. Chem. A*, 2014, **2**, 2623.
40 L. Lin, Q. Zhu and A. W. Xu, *J. Am. Chem. Soc.*, 2014, **136**, 11027–11033.
41 I. S. Amiinu, X. B. Liu, Z. H. Pu, W. Q. Li, Q. D. Li, J. Zhang, H. L. Tang, H. N. Zhang and S. C. Mu, *Adv. Funct. Mater.*, 2018, **28**, 1704638.
42 Z. Y. Wu, X. X. Xu, B. C. Hu, H. W. Liang, Y. Lin, L. F. Chen and S. H. Yu, *Angew. Chem., Int. Ed.*, 2015, **46**, 8179–8183.
43 F. Li, H. Li, X. Liu, L. Wang, Y. Lu and X. Hu, *Chem.–Eur. J.*, 2019, **25**, 635–641.
44 Y. Qiao, P. Yuan, Y. Hu, J. Zhang, S. Mu, J. Zhou, H. Li, H. Xia, J. He and Q. Xu, *Adv. Mater.*, 2018, **30**, 1804504.
45 U. I. Kramm, M. Lefevre, N. Larouche, D. Schmeisser and J. P. Dodelet, *J. Am. Chem. Soc.*, 2014, **136**, 978–985.
46 K. Yuan, S. Sfaelou, M. Qiu, D. Lützenkirchen-Hecht, X. Zhuang, Y. Chen, C. Yuan, X. Feng and U. Scherf, *ACS Energy Lett.*, 2017, **3**, 252–260.
47 H. Tan, J. Tang, J. Henzie, Y. Li, X. Xu, T. Chen, Z. Wang, J. Wang, Y. Ide, Y. Bando and Y. Yamauchi, *ACS Nano*, 2018, **12**, 5674–5683.
48 W. Gu, M. Wu, J. Sun, J. Xu and T. Zhao, *J. Mater. Chem. A*, 2019, **7**, 20132–20138.
49 L. Tong, Z. Shao, Y. Qian and W. Li, *J. Mater. Chem. A*, 2017, **5**, 3832–3838.
50 D. S. Xia, X. Yang, L. Xie, Y. P. Wei, W. L. Jiang, M. Dou, X. N. Li, J. Li, L. Gan and F. Y. Kang, *Adv. Funct. Mater.*, 2019, 1906174.

 